



HAL
open science

An open-source instrumentation package for intensive soil hydraulic characterization

Paola Concialdi, Simone Di Prima, Harsh Bhanderi, Ryan Stewart, Majdi Abou Najm, Murari Lal Gaur, Rafaël Angulo-Jaramillo, Laurent Lassabatère

► **To cite this version:**

Paola Concialdi, Simone Di Prima, Harsh Bhanderi, Ryan Stewart, Majdi Abou Najm, et al.. An open-source instrumentation package for intensive soil hydraulic characterization. *Journal of Hydrology*, 2020, 582, pp.124492. 10.1016/j.jhydrol.2019.124492 . hal-02438812

HAL Id: hal-02438812

<https://univ-lyon1.hal.science/hal-02438812>

Submitted on 5 Jan 2021

HAL is a multi-disciplinary open access archive for the deposit and dissemination of scientific research documents, whether they are published or not. The documents may come from teaching and research institutions in France or abroad, or from public or private research centers.

L'archive ouverte pluridisciplinaire **HAL**, est destinée au dépôt et à la diffusion de documents scientifiques de niveau recherche, publiés ou non, émanant des établissements d'enseignement et de recherche français ou étrangers, des laboratoires publics ou privés.

1 **An open-source instrumentation package for intensive soil hydraulic** 2 **characterization**

3 **Paola Concialdi**¹, **Simone Di Prima**^{2,3*}, **Harsh M. Bhanderi**⁴, **Ryan D. Stewart**⁵, **Majdi R. Abou Najm**⁶,
4 **Murari Lal Gaur**⁴, **Rafael Angulo-Jaramillo**² and **Laurent Lassabatere**²

5 ¹ University of Palermo, Department of Agricultural, Food and Forest Sciences, Palermo, Italy.

6 ² Université de Lyon; UMR5023 Ecologie des Hydrosystèmes Naturels et Anthropisés, CNRS, ENTPE, Université Lyon 1,
7 Vaulx-en-Velin, France.

8 ³ University of Sassari, Department of Agricultural Sciences, Sassari, Italy.

9 ⁴ College of Agricultural Engineering, Anand Agricultural University, Godhra, Gujarat, India.

10 ⁵ School of Plant and Environmental Sciences, Virginia Polytechnic Institute and State University, Blacksburg, VA,
11 United States.

12 ⁶ Department of Land, Air and Water Resources, University of California, Davis, CA 95616, United States.

13 * Corresponding Author. E-mail: sdiprima@uniss.it

14 **Abstract:** We present a new open-source and modular instrumentation package composed of up to ten
15 automatic infiltrometers connected to data acquisition systems for automatic recording of multiple infiltration
16 experiments. The infiltrometers are equipped with differential transducers to monitor water level changes in a
17 Mariotte reservoir, and, in turn, to quantify water infiltration rates. The data acquisition systems consist of
18 low-cost components and operate on the open-source microcontroller platform Arduino. The devices were
19 tested both in the laboratory and on different urban and agricultural soils in France and India. More
20 specifically, we tested three procedures to treat the transducers readings, including a filtering algorithm that
21 substantially improved the ability to determine cumulative infiltration from raw data. We combined these
22 three procedures with four methods for estimating the soil parameters from infiltrometer data, showing pros
23 and cons of each scenario. We also demonstrated advantages in using the automatic infiltrometers when
24 infiltration measurements were hindered by: i) linearity in cumulative infiltration curves owing to
25 gravity-driven flow, ii) an imprecise description of the transient state of infiltration, and iii) the occurrence of
26 soil water repellency. The use of the automatic infiltrometers allows the user to obtain more accurate estimates
27 of soil hydraulic parameters, while also reducing the amount of effort needed to run multiple experiments.

28 **Keywords:** automatic infiltrometer; infiltration rate measurements; soil hydraulic properties; Arduino.

29 **Highlights**

- 30 • We present an open-source instrumentation package for infiltration experiments.
- 31 • We tested the devices under challenging field conditions.
- 32 • We developed an algorithm for filtering the raw data recorded by transducers.

33 1. Introduction

34 Different automated devices have been developed to measure water infiltration rates in the field. Automation
35 strategies have involved the use of many different set-ups and sensors, including pressure transducers (e.g.,
36 Ankeny et al., 1988; Casey and Derby, 2002; Constantz and Murphy, 1987; Di Prima, 2015; Madsen and
37 Chandler, 2007; Prieksat et al., 1992), infrared sensor systems (Milla and Kish, 2006), micro flow-meters
38 (Moret-Fernández et al., 2012), reflectometry probes (Moret et al., 2004), and load cell sensors (Klípa et al.,
39 2015; Zumr et al., 2019). Among these approaches, pressure transducers are widely used for field applications
40 given their simplicity of use and low price. These sensors allow the user to monitor water level changes in a
41 Mariotte reservoir, and, in turn, to quantify water infiltration rates. Automation of a Mariotte reservoir was
42 firstly proposed by Constantz and Murphy (1987). These authors used a pressure transducer connected at the
43 top of a Mariotte reservoir to monitor the head-space tension during the drop of the water level. This technique
44 was used by Ankeny et al. (1988) to automate a tension infiltrometer for infiltration rates measurements under
45 negative suction. These authors tested two different set-ups: the first configuration had a single pressure
46 transducer located at the top of the Mariotte reservoir, while the second configuration added another pressure
47 transducer at the base of the water column. The use of two transducers overcame some of the difficulties
48 generated from the tension fluctuations caused by bubbling. This strategy was further improved by Casey and
49 Derby (2002), who used a differential transducer with two ports to automate an SW-080B tension infiltrometer,
50 and Madsen and Chandler (2007), who automated a mini-disk infiltrometer (Decagon, 2014) using pressure
51 transducers. Selker et al. (2009) incorporated pressure transducers and pneumatic reed switches to create a
52 tension infiltrometer with automated, near-instantaneous control over the tension applied to the water source.
53 Pressure transducers have also been used to automate single-ring infiltrometers (Prieksat et al., 1992).

54 The single-ring infiltrometer technique (Reynolds and Elrick, 1990) is a widespread method (e.g., Braud et al.,
55 2017), which has the advantages of speed and simplicity over more cumbersome procedures for performing
56 field-saturated soil hydraulic conductivity measurements, such as the Guelph permeameter and the double-ring
57 infiltrometer (Di Prima et al., 2019). These infiltrometers maintain a quasi-constant head in a containment ring,
58 allowing to calculate infiltration rates under ponding conditions (Angulo-Jaramillo et al., 2016). Recently, Di
59 Prima (2015) presented a new automated single-ring infiltrometer. This device is equipped with a differential
60 transducer to measure the stepwise drop of water level in a Mariotte reservoir. The data acquisition system
61 consists of low-cost components and uses the open-source Arduino microcontroller platform.

62 The potential of this automated infiltrometer to reliably derive saturated hydraulic conductivity, K_s , and
63 sorptivity, S , was tested by using three existing BEST algorithms, i.e., BEST-slope (Lassabatere et al., 2006),
64 BEST-intercept (Yilmaz et al., 2010) and BEST-steady (Bagarello et al., 2014). This approach demonstrated
65 that the total volume applied with the prototype version of the infiltrometer (130 mm) may not be sufficient to
66 evaluate steady state conditions, compromising the reliability of the estimates in some cases (e.g., loamy soil).
67 The importance to collect an appropriate number of data points during the transient state was investigated, using
68 analytically generated data, by increasing the precision of the collected information, namely decreasing the
69 cumulative infiltration interval from 5 mm to 2.5 mm. In the case of readings every 2.5 mm, the number of
70 points used to describe the same curve doubled and generated enough points to accurately model the transient
71 state of infiltration. Based on these results, Di Prima et al. (2016) proposed guidelines for the optimization of the
72 design in terms of capacity of the Mariotte reservoir (which affects the cumulative amount of infiltration that
73 can be measured) and the radius of air entry tube (which affects the increment size between two successive
74 measurements). These guidelines thus suggest ways to optimize infiltrometers to accurately measure transient
75 and steady-state infiltration conditions, yet the actual effectiveness of these improvements have not been
76 assessed using experimental data.

77 Another limitation on the use of the initial prototype is the need to filter raw data recorded by the transducer.
78 The transducer readings produce a step-shaped or stair-like relationship between time and recorded voltage.
79 These artifacts tend to be caused by air bubble formation in the Mariotte system, and the magnitude and rate of
80 change of the resulting steps tend to depend on the infiltrometer set-up. Di Prima (2015) and Di Prima et al.
81 (2016; 2017) manually processed the data, which complicated post-processing step and required a tremendous
82 amount of work and time to determine cumulative infiltration curves. While previous work has attempted to
83 ease the analysis of infiltration data from automated infiltrometers, for instance using the FLOWDATA
84 software developed by Ankeny et al. (1993), such methods are not able to filter out “stair-like” relationships that
85 are often obtained with the proposed infiltrometer.

86 Lastly, previous studies have shown that the strong spatial variability of hydraulic properties and water
87 infiltration at the field scale may affect measurement of water cumulative infiltration and related estimates for
88 hydraulic parameters (e.g., Zimmermann et al., 2008). For instance, Lassabatere et al. (2019a) developed the
89 concept of the BMR (Beerkan Multi Run) showing the need for a large dataset of experimental data for a proper
90 representation of the average response and its variability. Automated infiltrometers may be used to collect
91 simultaneous measurements at multiple locations for relatively long periods of time, thus providing accurate

92 data at high spatial and temporal resolutions. The use of automated infiltrometers may therefore improve
93 characterization of spatial variability in soil hydraulic characteristics, making it important to develop a system
94 that can collect and integrate measurements from multiple units

95 In this investigation we present a new modular instrumentation package, based on the original design of Di
96 Prima (2015), that has been updated to include up to ten automatic infiltrometers for automatic recording of
97 simultaneous infiltration experiments. Following the guidelines in Di Prima et al. (2016), we improved the
98 design of the devices in terms of reservoir capacity to ensure steady state at the end of the experiment, accuracy
99 of the description of the transient phase of the infiltration process, and number of infiltrometers that can be
100 simultaneously operated. This set of new devices should produce an optimum description of the cumulative
101 infiltration for an optimum hydraulic characterization. The main objectives of this paper were to: i) testing the
102 potential of the instrumentation package to automatically collect data from multiple infiltrometers working
103 simultaneously, ii) improving the treatment of the raw data recorded by the transducers, iii) assessing the use of
104 the infiltrometers in conjunction with different methods for estimating the soil parameters from infiltrometer
105 data, and iv) evaluating instrument performance under specific and challenging field conditions, such as highly
106 permeable, slightly sorptive and water repellent conditions

107 **2. Materials and Methods**

108 *2.1. Improved Infiltrometer design*

109 The main components of the complete system are illustrated in Figure 1. Each infiltrometer consists of a
110 Mariotte bottle with a 94-mm inner diameter and a height of 850 mm, with effective water storage height of 740
111 mm. It provides the capacity to hold the volume of water corresponding to a total cumulative infiltration of 280
112 mm based on a 150 mm infiltration ring diameter. This water volume represents 150 mm of additional water
113 available for infiltration compared to the prototype proposed by Di Prima (2015).

114 An air entry tube is positioned with its lower end at short distance from the reservoir base, which controls the air
115 entry in the Mariotte bottle and thus the water level inside the ring. The air entry tube has a 7 mm inner diameter,
116 compared to the 6.5 mm inner diameter used in the original prototype. Using this larger diameter tube changed
117 the cumulative infiltration interval from ~4.5 mm in the original prototype to ~2 mm in the updated version (see
118 section 3.3). This change was implemented with the goals of increasing the precision of the collected
119 information and allowing the collection of many data points during the first stage of the process.

120 The Mariotte bottle is closed by a top and a bottom plug (Figure 1c-e) and sustained through a tripod (Figure
121 1f-g) made of four interlocking parts (3 legs and 1 circular support). The design of the tripod allows the user to
122 easily regulate the distance between the base of the infiltrometer and the infiltration surface, with an adjustable
123 range from 2-3 mm at the closest setting up to 90 mm at the most distant setting. The tripod components were
124 manufactured through an online laser cutting service. This type of service is offered by a number of online
125 companies, which typically allow users to choose the thickness and the type of material and then upload a file
126 (e.g., .eps, .svg or .dxf) that specifies the cutting lines. An illustration of the cutting lines is provided in Figure
127 1f. The plugs can be realized by different 3D printing technologies, such as stereolithography (SLA), selective
128 laser sintering (SLS), and Multi Jet Fusion (MJF). The project files for the realization of the plugs (Figure 1c)
129 and the tripod (Figure 1f) can be downloaded from the website bestsoilhydro.net. We note that online
130 manufacturer services tend to be cost-effective, allowing the user to build the system for relatively low cost.

131 2.2. *Data acquisition system and differential pressure sensor*

132 The core of the data acquisition system consists of an Arduino Mega microcontroller board, an Arduino
133 wireless shield with an onboard micro-SD socket and a LCD module shield (20 columns and 4 rows) and a
134 differential pressure transducer. The list of components and the Arduino code can be downloaded from the
135 website bestsoilhydro.net. The LCD module requires that a specific library (LiquidCrystal_I2C) be installed
136 into the Arduino IDE; this library can be downloaded from the website wiki.sunfounder.cc. The data acquisition
137 system (Figure 1b) is connected to differential pressure sensors (Figure 1a) using 3-m-long cables. Each system
138 simultaneously connects to as many as five infiltrometers. The differential pressure sensor box is mounted on
139 the top of the infiltrometer (Figure 1d). The two ends of the transducer are connected using small plastic flexible
140 tubes (outer diameter = 4 mm) to the head-space of the reservoir and to an acrylic tube (outer diameter = 10 mm,
141 inner diameter = 7 mm, height = 790 mm) descending inside the reservoir. This configuration enables
142 measurement of the pressure difference between the head-space and the bottom of the column of water. The
143 differential pressure transducer used for this application is the piezoresistive differential pressure transducer
144 MPXV5010DP, from NXP semiconductors (nxp.com; other companies that provide similar transducers include
145 SMI and Honeywell). This sensor requires a power supply of 5 V and has an integrated temperature
146 compensation and signal amplification circuit. The transducer provides a linear voltage output for a differential
147 pressure range from 0 to 1000 mm H₂O. The data are recorded on a SD card and simultaneously displayed on
148 the LCD display. The software generates a new comma-separated values (CSV) file every time that the
149 microcontroller is activated. The name of the generated file appears on the LCD.

150 2.3. *Infiltrometer system calibration*

151 Laboratory calibration of the devices was carried out by visually monitoring the height of the water column
152 inside the Mariotte bottle during the complete emptying of the reservoirs. Each infiltrometer was placed within
153 a 150-mm inner diameter cylinder; a quasi-constant water head of 5 mm was maintained inside the cylinder.
154 Visual readings of the water levels were done on a 740-mm long ruler with the zero positioned 10 mm above the
155 bottom end of the tube connected to the pressure side of the differential pressure sensor. Then, a calibration
156 function was created via linear regression between the visual readings of the heights of the water column and the
157 corresponding recorded volts. The calibration function for each infiltrometer was used in subsequent
158 experiments to convert recorded transducer outputs into water column heights, which were then used to
159 estimate infiltration amounts.

160 2.4. *Laboratory testing*

161 All of the infiltrometers were also tested in the laboratory (example shown in Figure 2). Similar to the
162 calibration procedure, the infiltrometer was used to maintain a quasi-constant head of water inside a 150-mm
163 inner diameter cylinder that was connected via an outlet pipe to a collection container set on a balance (Figure
164 2a). The experiments were carried out by recording the transducer output during the complete emptying of the
165 reservoir while weighing the mass of discharged water (Figure 2a and b). In the example of Infiltrometer #3, the
166 transducer voltage was constant during intervals where bubbles form in the air-entry tube, reflecting a constant
167 water level in the reservoir. Once a bubble reached sufficient size to enter the water column, e.g., at time
168 $t = 509$ s (observations in Figure 2b and left-most red triangle in Figure 2c), the transducer readings fluctuated
169 and generated easily detectable outliers (blue solid circles in Figure 2c), as already discussed by Ankeny et al.
170 (1988). The transducer readings then stabilized at a constant value until the subsequent bubbling event, e.g., the
171 transducer output stayed at 2.85 V between $t = 510$ and 517 s. As highlighted by Di Prima (2015) and Di Prima
172 et al. (2016), this typically behavior produces a step-shaped relationship between time and recorded voltage
173 (Figure 2c).

174 2.5. *Field testing*

175 After laboratory calibration and testing, we also tested the devices during four experimental campaigns in the
176 field, with three sites in France and one in India. The first two sites (ENTPE-1 and ENTPE-2 sites) are located in
177 the garden of the École Nationale des Travaux Publics de l'État (ENTPE) in the municipality of Vaulx-en-Velin
178 (France). The third site (DOUA site) is a drainage ditch located at the La DOUA scientific campus in the

179 municipality of Villeurbanne (France), which receives runoff mainly originating from adjacent parking lots and
180 sidewalks. These municipalities belong to the Metropolis of Lyon in Auvergne-Rhône-Alpes region in eastern
181 France. The three sites are part of the Lyon city Field Observatory for Urban Water Management (OTHU). The
182 sampled soils ranged in texture from silt to sand (Bouarafa et al., 2019). The fourth experimental site is a sandy
183 loam soil covered by maize crop that is located at the Anand Agricultural University in the western Indian state
184 of Gujarat.

185 For each site in France, a total of four undisturbed soil cores (50 mm in height and 50 mm in diameter) were
186 collected at randomly sampled points and used to determine both the soil bulk density, ρ_b (g cm^{-3}), and the initial
187 volumetric soil water content, θ_i ($\text{cm}^3 \text{cm}^{-3}$) (Table 1). We used the infiltrometers to carry out a total of fifteen
188 infiltration experiments, with five simultaneous experiments conducted at each French site (Figure 3a). We
189 used stainless steel rings with an inner diameter of 150 mm, inserted shallowly into the soil (~10 mm) according
190 to the Beerkan procedure for single-ring infiltration experiments (Lassabatere et al., 2006). Following the
191 procedure described in Di Prima et al. (2016), we firstly positioned a plastic film on the soil surface inside each
192 ring and applied a small water head of few millimeters (2-3 mm), depending on the surface roughness. The
193 plastic film was also used to minimize disturbance on the soil surface while establishing ponding conditions and
194 to have an accurate data acquisition from the beginning of the run. The infiltrometers were positioned inside the
195 rings and regulated in height so that the bases were in contact with the ponding water. The Mariotte bottles were
196 filled with tap water and then activated through lifting the pistons. A few seconds after flow began, the data
197 acquisition was started by simply switching on the data acquisition system. Finally, the infiltration experiments
198 started when the plastic films were removed. A video tutorial showing this procedure can be viewed online (Di
199 Prima, 2014). At the ENTPE-1 site, we also used all the automatic infiltrometers connected to two data
200 acquisition systems for automatic recording of ten simultaneous infiltration experiments. These experiments
201 were aimed to test the potential of the proposed instrumentation package to capture soil heterogeneity.

202 The hypothesis of an improved description of the cumulative infiltration curve was investigated through a
203 comparison with the prototype proposed by Di Prima (2015). At this aim, we made a comparison between 45
204 curves collected with the prototype during previous field campaigns (Di Prima, 2015; Di Prima et al., 2017,
205 2016), and the curves collected with new infiltrometers at the ENTPE-1, ENTPE-2 and DOUA sites.

206 At the experimental site in India, we conducted a total of six infiltration experiments. Three runs of the
207 double-ring type were carried out using an inner ring of 150 mm diameter and outer ring of 300 mm diameter.
208 The automatic infiltrometer was used to maintain constant water depths in the inner rings of 25 mm (Run 1), 50

209 mm (Run 2), and 75 mm (Run 3), while the same water depths were maintained in the outer ring manually by
 210 pouring the water during the experiments. Assuming that water infiltration below the inner ring was
 211 one-dimensional (1D) and that the final steady flow was only gravity driven, we estimated the saturated soil
 212 hydraulic conductivity based on the steady infiltration rate (Reynolds et al., 2002a). The other three runs used
 213 single rings with 150 mm inner diameter. The infiltrometers were used to maintain constant depths of 25 mm
 214 (Run 4), 50 mm (Run 5), and 75 mm (Run 6).

215 2.6. Treatment of the raw data recorded by the transducers

216 In this investigation, we propose three different procedures to treat the raw data recorded by the transducer. The
 217 first procedure, proposed by Di Prima (2015) and applied by Di Prima et al. (2016; 2017), requires the user to
 218 manually select values at the end of the constant height stages, i.e., by sampling the transducer readings at time
 219 immediately preceding the bubbling. The second procedure automatically selects these values through an
 220 algorithm coded with the open-source software Scilab. The code can be downloaded from the website
 221 bestsoilhydro.net. Because the code may fail in certain cases owing to unpredictable noise in the transducer
 222 readings, in this investigation we decided to apply both procedures. Further, these two procedures cannot be
 223 adopted whenever rapid emptying of the Mariotte bottle causes uninterrupted air bubbling, which may occur
 224 during high infiltration rates (Di Prima et al., 2016). Following the suggestion by Di Prima et al. (2016), we
 225 therefore applied a third procedure that calculated a moving median to identify the underlying trend of
 226 transducer output with time. In the laboratory, the accuracy of these procedures was evaluated through the
 227 comparison between recorded and measured cumulative flow data (Figure 2d) in terms of relative error, Er (%),
 228 and root mean squared differences, $RMSD$ (mm), defined as:

$$229 \quad Er = 100 \times \sqrt{\frac{\sum_{i=1}^n (I_i^{exp} - I_i)^2}{\sum_{i=1}^n (I_i^{exp})^2}} \quad (1)$$

$$230 \quad RMSD = \sqrt{\frac{\sum_{i=1}^n (I_i^{exp} - I_i)^2}{n}} \quad (2)$$

231 where n is the total number of data pairs, I_i^{exp} (mm) are the measured data, estimated from the mass of
 232 discharged water during laboratory tests, and I_i (mm) are the values estimated from the recorded transducer

233 data using the calibration functions. Also, the recorded total cumulative flow, I_{tot} (mm), were compared with
234 the corresponding measured data, I_{tot}^{exp} (mm), using the relative error, $Er(I_{tot})$ (%), defined as follows:

$$235 \quad Er(I_{tot}) = 100 \times \frac{I_{tot} - I_{tot}^{exp}}{I_{tot}^{exp}} \quad (3)$$

236 The three procedures presented above to treat the transducer output (i.e., manual selection, automatic selection
237 and moving median) were subsequently applied to determine the cumulative infiltration curves. In addition, we
238 also considered a fourth procedure described below. According to Angulo-Jaramillo et al. (2016), an expected
239 advantage of the use of the automatic infiltrometers is better accuracy during the transient flow state. In this
240 paper we investigated this hypothesis by processing the raw data in order to obtain “Beerkan-like data”, i.e.,
241 cumulative infiltration curves having the same increments (8.5 mm) as manually pouring water volumes into
242 the containment ring. More specifically, the curves obtained by manually sampling the transducer readings
243 were further processed and polynomial regression functions were applied to cumulative data to model the
244 discretized infiltration measurements.

245 *2.7. Estimating hydrodynamic parameters from field experiments*

246 All the cumulative infiltration curves from the four different procedures were subsequently inverted by three
247 different approaches to estimate the soil sorptivity, S ($\text{mm h}^{-0.5}$) and the saturated hydraulic conductivity, K_s
248 (mm h^{-1}). The three approaches represented different algorithms within the Beerkan Estimation of the Soil
249 Transfer parameters (BEST) solution introduced by Lassabatere et al. (2006), Yilmaz et al. (2010), and
250 Bagarello et al. (2014), and differed from one another in the manner by which they fit the experimental
251 cumulative infiltration to the approximate expansion for transient and steady states defined by Haverkamp et al.
252 (1994) and to derive S and K_s . More specifically, BEST-slope (Lassabatere et al., 2006) uses the slope of the
253 straight line defined by the last points (representative of the steady state) to constrain S and K_s , before fitting the
254 transient model to the experimental data by the optimization of S . BEST-intercept (Yilmaz et al., 2010) uses the
255 intercept of the steady state model to constrains S and K_s , priori fitting the experimental data. Lastly,
256 BEST-steady (Bagarello et al., 2014) uses both the slope and the intercept to resolve a set of two equations (Di
257 Prima et al., 2016), leading to the estimation of the two unknowns, S and K_s . More information on BEST can be
258 found in Angulo-Jaramillo et al. (2019).

259 K_s values were also estimated using Approach 4 in Stewart and Abou Najm (2018), in which the macroscopic
260 capillary length, λ , was assumed to have a constant value of $\lambda = 150$ mm, following the recommendation of
261 Stewart and Abou Najm (2018). Note that this approach does not require additional information (e.g., particle

262 size distribution, initial and final soil water content and dry soil bulk density) to estimate K_s from infiltration
263 runs. Therefore, it is particularly useful when a large number of locations needs to be sampled, particularly
264 when time and financial resources are limited (Di Prima et al., 2019). At the Indian site, K_s values were
265 estimated using Approach 4, as this method is also usable for both quasi-zero (i.e., the French sites) and positive
266 values (Indian site) of ponded depth on the infiltration surface.

267 **3. Results and discussion**

268 3.1. *Calibration and Laboratory testing*

269 Each infiltrometer had a unique calibration function between the visual readings of the water column heights
270 and the corresponding voltage recorded during the emptying of the Mariotte bottle (Table 2). All transducers
271 provided a nearly linear relationship between the voltage output and the heights of the water columns; as an
272 example, $R^2 = 1.0$ for the calibration relationship collected using Infiltrator #3 (Figure 4, Table 2). They also
273 had nearly identical values of the calibration multiplier ranging from 4.32×10^{-3} and 4.36×10^{-3} V/mm H_2O ,
274 while, as also noted by Ankeny (1992), the intercept yielded more variable values ranging from 0.328 and 0.390
275 mm. Nonetheless, while the calculation of the water levels is affected by the intercept value, the calculation of
276 the water volume change between readings is independent from this parameter. However, the intercept value is
277 still useful to exclude the water levels measured below the zero of the rule from the calculation of the water
278 volumes, as the internal geometry of the Mariotte bottles changes below this level (Figure 2a). In the laboratory,
279 the accuracy of the three procedures to treat the transducer output (i.e., manual selection, automatic selection
280 and moving median) was evaluated through a comparison between recorded and measured cumulative flow
281 data. All procedures yielded small errors (Table 3), suggesting that the ten infiltrometers had good accuracy
282 when measuring water flow. More specifically, the three procedures yielded *RMSD* ranging between 0.41 and
283 3.06 mm, *Er* between 0.28 and 2.06%, and $Er(I_{tot})$ between 0.06 and 1.76%. The three procedures did not yield
284 significantly different errors (Table 3 and Figure 5). This result suggests that adopting a simplified procedure to
285 treat the transducer output, such as a moving median, does not negatively affect determination of flow data. In
286 addition, the laboratory experiments, with a quasi-constant head of water maintained inside a cylinder, allowed
287 us to test the infiltrometers with a similar set-up to that one used on the field, thus increasing our confidence in
288 the field measurements.

289 3.2. *Field testing*

290 3.2.1. *Optimum case and peculiarities*

291 Cumulative infiltration into an unsaturated porous medium typically exhibits a concave shape as a function of
292 time, due to a decreasing hydraulic gradient as the wetting front moves away from the source and the influence
293 of capillarity decreases (Xu et al., 2012). As flow rates approach steady state, cumulative infiltration becomes
294 approximately linear with time (Angulo-Jaramillo et al., 2016). An example of this behavior is depicted in
295 Figure 6a-e. In this example, the measured infiltration rates showed the typical stepwise drop in water level
296 within the reservoir, yielding the same kind of stair-like output (Figure 6a) as the one reported for the laboratory
297 experiments (Figure 2c). All three procedures used to treat the transducer output (i.e., manual selection,
298 automatic selection and moving median) were successfully applied to these data (Figure 6c and e) and yielded
299 similar cumulative infiltration curves as one another (Figure 6b). Besides, all combinations of treatment
300 procedure and characterization algorithms gave similar results for this example. This result suggests that in case
301 of stair-like output, using the automatic procedure to treat the raw data is preferable, given that it avoids the
302 tremendous amount of work and time required when manually processing the data.

303 The success of this example case above did not translate to all infiltration tests. Certain combinations of data
304 treatment procedures and soil characterization algorithms failed to successfully characterize soil properties,
305 yielding success rates as low as 40% for the manual selection method combined with BEST-slope (Table 4,
306 Figure 7a).

307 Further, for each site and treatment procedure, the four methods (i.e., BEST-slope, BEST-intercept,
308 BEST-steady and Approach 4) provided different success rates (Table 4). These differences then carried over to
309 the overall distributions for K_s (Figure 7b) and S (Figure 7c). Thus, as demonstrated by these results, different
310 assumptions and analysis structures inherent to the four methods and three alternative procedures used to treat
311 the transducer output (i.e., manual selection, automatic selection and moving median) makes each combination
312 sensitive to different kinds of non-ideal conditions. Below we discuss different types of obstacles that may
313 commonly hinder infiltration measurements in the field, including: i) linearity in cumulative infiltration curves
314 owing to gravity-driven flow, ii) imprecise description of the transient state of infiltration, and iii) occurrence of
315 soil water repellency. We also discuss related advantages provided by automatic infiltrometers when dealing
316 with these issues.

317 3.2.2. *High flow rate experiments*

318 For six out of fifteen experiments, the infiltration processes were entirely dominated by the influence of
319 preferential flow paths, with infiltration rates ranging between 1529.8 and 5215.1 mm h⁻¹ (as estimated by the
320 moving median approach). In such circumstances, we distinguished two different scenarios depending on the
321 rapidity of the process. In three cases (first scenario), one at the ENTPE-1 site and two at the DOUA site, we
322 measured infiltration rates equal or lower than 3159.3 mm h⁻¹ (Table 4). Still, the rapid infiltration process and
323 the high measured infiltration rates did not cause uninterrupted bubbling within the Mariotte bottle. Therefore,
324 the emptying process was characterized by the typical stepwise drop of water level in the reservoirs, yielding the
325 same kind of stair-like output reported previously (Figure 2c and Figure 6a), and all the three procedures to treat
326 the transducer output were successfully applied. However, the influence of preferential flow paths on the
327 infiltration processes made it impossible to evaluate any effect of the capillary flow. Obviously, in such
328 condition the use of transient models to fit infiltration data was inappropriate, and BEST-slope and
329 BEST-intercept failed to provide S and K_s values (Lassabatere et al., 2019b). Three other experiments at the
330 DOUA sites yielded even higher infiltration rates, ranging from 3496.3 and 5215.1 mm h⁻¹ (second scenario).
331 Under these conditions, the manual and automatic procedures to treat the raw data could not be applied owing to
332 the rapid emptying of the Mariotte bottle causing an uninterrupted air bubbling that spoiled the transducer
333 readings (Figure 6h and i; also discussed in Di Prima et al., 2016). On the contrary, the application of a moving
334 median successfully revealed the underlying trend of the transducer output with time (Figure 6f and j), thus
335 allowing cumulative infiltration to be determined (Figure 6g). It also should be noted that, when the infiltration
336 process was mainly driven by gravity and cumulative infiltration curves were near-linear (Lassabatere et al.,
337 2019b), BEST-slope and BEST-intercept failed to provide S and K_s estimates, while BEST-steady was
338 successfully applied. Indeed, according to Bagarello et al. (2014), BEST-steady does not require data from the
339 transient stage of the run but rather relies solely on the regression analysis of the final few cumulative
340 infiltration depths. This particular algorithm avoided the uncertainties due to the linearity of the cumulative
341 infiltration, which can obscure the distinction between the early- and late-time infiltration processes (Di Prima
342 et al., 2018).

343 3.2.3. *Improved description of the transient phase*

344 The hypothesis of a better description of the transient phase when using the automatic infiltrometers was
345 investigated through a comparison between the cumulative infiltration curves obtained from transducer output
346 and discretized curves having the same increments as manually pouring water volumes into the containment
347 ring. In the reported example (Figure 8), the infiltration reached steady state early (i.e., within the first 0.03 h)

348 and only one discretized data point occurred within the transient flow regime. As a consequence, the transient
349 infiltration models in BEST-slope and BEST-intercept could not be fitted to the discretized data. Conversely,
350 the high-resolution cumulative infiltration curve obtained from the transducer output captured 14 points during
351 the transient state, allowing for the BEST-slope (Figure 8c) and BEST-intercept algorithms to be fitted. In some
352 cases, too few points could be identified for the description of the transient state. Such a problem occurred at the
353 ENTPE-1 site, likely due to the high local initial soil water content there (Table 1). In addition to this example,
354 BEST-slope also failed in two cases at the ENTPE-2 site whereas BEST-intercept was successfully applied;
355 consequently, the former method had the lowest success rate (Figure 7). This shortcoming was already
356 investigated in several investigations (e.g., Castellini et al., 2018; Di Prima et al., 2018). More specifically,
357 when the early- and late-time infiltration stages greatly differ in terms of infiltration rates, the strong concavity
358 of cumulative infiltration results in an over-estimation of soil sorptivity. Such overestimations result in negative
359 values for K_s , as already suggested by Yilmaz et al. (2010).

360 3.2.4. *Water repellent soils*

361 The first obvious advantage in using automatic infiltrometer in case of water repellent soils is that data
362 collection is automated and it does not require any further manipulation by the user once the device is installed.
363 Therefore, tests can be successfully (and simultaneously) performed even if water repellency impedes
364 infiltration and causes long testing durations (Alagna et al., 2018). In addition, the automatic infiltrometer used
365 in this investigation was capable of maintaining a small water head on the soil surface, which helps to prevent
366 excessive positive pressure from overcoming the soil water repellency (Nyman et al., 2010). For one
367 experiment at the ENTPE-1 site, this experimental approach was useful to signal the occurrence of soil water
368 repellency, as identified by cumulative infiltration having a convex curve shape (Di Prima et al., 2017). The
369 cumulative infiltration data in that instance yielded a negative value for the intercept of the regression line fitted
370 to the data points describing steady-state conditions (e.g., Alagna et al., 2018; Di Prima et al., 2019, 2017;
371 Lozano-Baez et al., 2018). This circumstance led to the failure of all the BEST-algorithms (Lassabatere et al.,
372 2019a); only Approach 4 provided an estimate of K_s . More specifically, BEST-slope and BEST-intercept failed
373 because both algorithms required fitting transient models to early infiltration data that must be concave instead
374 of convex as determined by soil water repellency. The BEST-steady algorithm avoids most problems associated
375 with the use of the transient infiltration data, yet still estimates meaningless K_s data in case of negative intercept
376 values. On the other hand, Approach 4 by Stewart and Abou Najm (2018) differs by the term expressing
377 steady-state condition, considering exclusively the final infiltration rate, i.e., the slope of regression line fitted to

378 the last data points of the cumulative infiltration. The exclusive use of this term allowed to consider only the
379 final stage of the infiltration process, i.e., when the water repellency had diminished or no effect on infiltration.
380 Therefore, we suggest to use steady state methods, such as Approach 4, in case of water repellent soils
381 (Angulo-Jaramillo et al., 2019). This example also illustrates that, when the physics of infiltration change, as in
382 the case of water infiltration into water repellent soils, all the BEST methods are questionable (Bauters et al.,
383 2003).

384 3.3. *Comparison with the prototype*

385 We also compared the cumulative infiltrations curves collected using the new infiltrometers with those
386 measured by the prototype proposed by Di Prima (2015) on different soils analyzed during previous field
387 campaigns (Di Prima, 2015; Di Prima et al., 2017, 2016). Figure 9 depicts a comparison between 45 curves
388 collected with the prototype (Figure 9a) versus the curves collected with new infiltrometers at the ENTPE-1,
389 ENTPE-2 and DOUA sites (Figure 9b). The mean value of the cumulative infiltration intervals, ΔI , decreased
390 from 4.65 mm with the original prototype to 2.15 mm with the new version (Figure 9c). Therefore, the new
391 infiltrometers had more than twice the resolution (i.e., shorter increments between readings) of the prototype.
392 Returning the example shown in Figure 8, the updated version of the automated infiltrometer provided 14
393 measurements during the transient regime (Figure 8c), whereas the prototype would only have the capability to
394 capture 3-4 points. Accurately modeling the transient state requires a minimum of five measurements
395 (Angulo-Jaramillo et al. 2019), meaning that the prototype system would be inadequate in that scenario. At the
396 same time, the new devices were able to collect measurements for longer durations (and greater cumulative
397 infiltration amounts) due to their larger storage capacity. Thus, compared to the prototype system the new
398 version of the infiltrometer can generate more data points during both transient and steady-state flow regimes.

399 3.4. *Application of the proposed device to double-ring measures*

400 An automatic infiltrometer constructed at the Anand Agricultural University was used to run both of the single-
401 and double-ring infiltration experiments. K_s values ranged between 15.0 and 105.8 mm h⁻¹ (Table 5). The
402 different experimental set-ups, including multiple imposed water depths (25, 50 and 75 mm), showed the
403 versatility of the device to execute experiments with multiple positive water heads, such as the one requested for
404 the two- or multiple-ponding-depth approaches (Reynolds and Elrick, 2002). For the double-ring experiments,
405 the use of the infiltrometer to maintain the water level in the inner ring improved monitoring of the infiltration
406 process while reducing the amount of effort needed to maintain a constant depth of water in both rings (Lai and

407 Ren, 2007). The main advantage of using the automated infiltrometer in this scenario was its simplicity, in that
408 it allowed a single operator to carry out the field experiments. In addition, the limited cost of the device means
409 that it can contribute to more widespread applications of accurate and automated infiltration rates
410 measurements, even when combined with cumbersome experiments such as the double-ring infiltrometer.

411 3.5. *On the advantage of multiple infiltration experiments*

412 The ability of the proposed instrumentation package to automatically collect data from up to ten infiltrometers
413 working simultaneously, i.e., when using ten infiltrometers connected to two data acquisition systems, was
414 tested at the ENTPE-1 site (Figure 10). Such a protocol had many advantages. Indeed, ten replicates enabled the
415 identification of specific runs, revealing either the effect of preferential flow (e.g., Figure 10b, run n. 10) or, on
416 the contrary, the impedance of flux owing to water repellency (e.g., Figure 10b, runs n. 4 and 8). In addition, ten
417 replicates should be appropriate to obtain representative mean values of soil hydrodynamic parameters at the
418 field scale (Reynolds and Elrick, 2002; Verbist et al., 2010). This protocol can help to overcome uncertainties in
419 the hydraulic characterization of highly heterogeneous soils. The new instrumentation package may constitute a
420 valuable tool for the application of the Beerkan multi-runs procedure proposed by Lassabatere et al. (2019a),
421 which consists in carrying out ten Beerkan infiltration experiments along a transect. The use of the automatic
422 infiltrometers in this protocol may both provide sufficient water supply to reach steady state and provide
423 measurement resolution needed to improve the description of the transient state. These advances allow the user
424 to obtain more accurate estimates of soil hydraulic parameters, while also reducing the amount of effort needed
425 to run multiple experiments.

426 4. Summary and conclusions

427 In this investigation we designed and manufactured a set of ten devices that automatically provide water at a
428 constant head and record the resulting infiltration rates. The design of the devices was improved over a
429 previously presented prototype in terms of reservoir capacity (which controls the duration of the test), diameter
430 of the air entry tube (which controls the measurement resolution and corresponding accuracy of infiltration
431 measurements), and number of infiltrometers that can be simultaneously operated (here up to ten at one time).
432 We also proposed a new algorithm for the automatic processing of the transducer readings, which substantially
433 reduced the amount of work necessary to analyze the raw data. We encourage the readers to check the website
434 bestsoilhydro.net for the latest updates, and also to download: Arduino sketches, electronic schemes, codes for
435 data treatment, lists of components, models for 3D printing and laser cutting projects.

436 The devices were firstly tested in the laboratory and then on four different experimental sites under specific and
437 challenging field conditions, such as highly permeable, slightly sorptive and water repellent conditions. The
438 field campaigns highlighted the ease of use of the devices when performing either single-ring or double-ring
439 infiltration experiments. The new instrumentation package provided in this study allows the user to intensively
440 measure soil infiltration rates, with the capability of automatically recording multiple experiments. Automated
441 measurements also facilitate better detection of preferential flow and soil water repellency conditions in the
442 field.

443 **Author Contributions:** P. Concialdi and S. Di Prima realized the devices, outlined the investigation and
444 carried out the experimental activity in France. H. Bhanderi realized the device and carried out the experimental
445 activity at the Anand Agricultural University. L. Lassabatere coded the algorithm in Scilab for the automatic
446 treatment of the transducer output. All authors contributed to discussing the results and writing the manuscript.

447 **Funding:** This work was supported through the INFILTRON Project (ANR-17-CE04-0010, Package for
448 assessing infiltration & filtration functions of urban soils in stormwater management; <https://infiltron.org/>)
449 funded by the French National Research Agency (ANR). Funding was also provided in part by the Virginia
450 Agricultural Experiment Station and the Hatch Program of the National Institute of Food and Agriculture, U.S.
451 Department of Agriculture, and the European Regional Development Fund (ERDF) and the Italian Ministry of
452 Education, University and Research (MIUR) through the “Programma Operativo Nazionale (PON) Ricerca e
453 Innovazione 2014-2020 (Linea 1 - Mobilità dei ricercatori, AIM1853149, CUP: J54I18000120001).

454 **Acknowledgments:** The authors wish to thank the Lyon city Field Observatory for Urban Water Management
455 (OTHU), the Department of Agricultural, Food and Forest Sciences of the University of Palermo (Italy), and
456 Pier Nicola Labate and Andrea Melis from the laboratory FabLab UniSS of the University of Sassari (Italy) for
457 technical and scientific support. S.D.P. also thanks labandadipalermo.it for their contribution to keep the spirit
458 up.

459 **Conflicts of Interest:** The authors declare no conflict of interest.

460 5. References

- 461 Alagna, V., Iovino, M., Bagarello, V., Mataix-Solera, J., Lichner, E., 2018. Alternative
462 analysis of transient infiltration experiment to estimate soil water repellency.
463 Hydrological Processes. <https://doi.org/10.1002/hyp.13352>
464 Angulo-Jaramillo, R., Bagarello, V., Di Prima, S., Gosset, A., Iovino, M., Lassabatere, L.,
465 2019. Beerkan Estimation of Soil Transfer parameters (BEST) across soils and

466 scales. *Journal of Hydrology* 576, 239–261.
467 <https://doi.org/10.1016/j.jhydrol.2019.06.007>

468 Angulo-Jaramillo, R., Bagarello, V., Iovino, M., Lassabatère, L., 2016. Infiltration
469 Measurements for Soil Hydraulic Characterization. Springer International
470 Publishing.

471 Ankeny, M.D., Kaspar, T.C., Horton, R., 1988. Design for an Automated Tension
472 Infiltrometer. *Soil Science Society of America Journal* 52, 893.
473 <https://doi.org/10.2136/sssaj1988.03615995005200030054x>

474 Ankeny, M.D. (National S.T.L., 1992. Methods and theory for unconfined infiltration
475 measurements. SSSA special publication series (USA) 123–141.

476 Ankeny, M.D., Prieksat, M.A., Kaspar, T.C., Noh, K.M., 1993. FLOWDATA: Software for
477 Analysis of Infiltration Data from Automated Infiltrimeters. *Agronomy Journal* 85,
478 955–959. <https://doi.org/10.2134/agronj1993.00021962008500040030x>

479 Bagarello, V., Di Prima, S., Iovino, M., 2014. Comparing Alternative Algorithms to Analyze
480 the Beerkan Infiltration Experiment. *Soil Science Society of America Journal* 78,
481 724. <https://doi.org/10.2136/sssaj2013.06.0231>

482 Bauters, T.W.J., Steenhuis, T.S., DiCarlo, D.A., Nieber, J.L., Dekker, L.W., Ritsema, C.J.,
483 Parlange, J.Y., Haverkamp, R., 2003. Physics of hydrophobic soils. *Soil Water*
484 *Repellency: Occurrence, Consequences, and Amelioration* 215–224.
485 <https://doi.org/10.1016/B978-0-444-51269-7.50022-9>

486 Bouarafa, S., Lassabatere, L., Lipeme-Kouyi, G., Angulo-Jaramillo, R., 2019.
487 Hydrodynamic Characterization of Sustainable Urban Drainage Systems (SuDS) by
488 Using Beerkan Infiltration Experiments. *Water* 11, 660.
489 <https://doi.org/10.3390/w11040660>

490 Braud, I., Desprats, J.-F., Ayrat, P.-A., Bouvier, C., Vandervaere, J.-P., 2017. Mapping
491 topsoil field-saturated hydraulic conductivity from point measurements using
492 different methods. *Journal of Hydrology and Hydromechanics* 65.
493 <https://doi.org/10.1515/johh-2017-0017>

494 Casey, F.X.M., Derby, N.E., 2002. Improved design for an automated tension infiltrometer.
495 *Soil Sci. Soc. Am. J.* 66, 64–67.

496 Castellini, M., Di Prima, S., Iovino, M., 2018. An assessment of the BEST procedure to
497 estimate the soil water retention curve: A comparison with the evaporation method.
498 *Geoderma* 320, 82–94. <https://doi.org/10.1016/j.geoderma.2018.01.014>

499 Constantz, J., Murphy, F., 1987. An Automated Technique for Flow Measurements from
500 Mariotte Reservoirs1. *Soil Science Society of America Journal* 51, 252.
501 <https://doi.org/10.2136/sssaj1987.03615995005100010051x>

502 Decagon, 2014. Minidisk Infiltrometer User's Manual. Decagon Devices, Inc., Pullman,
503 USA 24.

504 Di Prima, S., 2015. Automated single ring infiltrometer with a low-cost microcontroller
505 circuit. *Computers and Electronics in Agriculture* 118, 390–395.
506 <https://doi.org/10.1016/j.compag.2015.09.022>

507 Di Prima, S., 2014. A new automated single ring infiltrometer for Beerkan infiltration
508 experiments [<https://www.youtube.com/watch?v=2nok8MJWV9s>].

509 Di Prima, S., Bagarello, V., Angulo-Jaramillo, R., Bautista, I., Cerdà, A., del Campo, A.,
510 González-Sanchis, M., Iovino, M., Lassabatere, L., Maetzke, F., 2017. Impacts of
511 thinning of a Mediterranean oak forest on soil properties influencing water
512 infiltration. *Journal of Hydrology and Hydromechanics* 65, 276–286.
513 <https://doi.org/10.1515/johh-2017-0016>

514 Di Prima, S., Castellini, M., Abou Najm, M.R., Stewart, R.D., Angulo-Jaramillo, R.,
515 Winiarski, T., Lassabatere, L., 2019. Experimental assessment of a new
516 comprehensive model for single ring infiltration data. *Journal of Hydrology* 573,
517 937–951. <https://doi.org/10.1016/j.jhydrol.2019.03.077>

518 Di Prima, S., Concialdi, P., Lassabatere, L., Angulo-Jaramillo, R., Pirastru, M., Cerda, A.,
519 Keesstra, S., 2018. Laboratory testing of Beerkan infiltration experiments for
520 assessing the role of soil sealing on water infiltration. *CATENA* 167, 373–384.
521 <https://doi.org/10.1016/j.catena.2018.05.013>

522 Di Prima, Simone, Lassabatere, L., Bagarello, V., Iovino, M., Angulo-Jaramillo, R., 2016.
523 Testing a new automated single ring infiltrometer for Beerkan infiltration
524 experiments. *Geoderma* 262, 20–34. <https://doi.org/10.1016/j.geoderma.2015.08.006>

525 Di Prima, S., Lassabatere, L., Bagarello, V., Iovino, M., Angulo-Jaramillo, R., 2016. Testing
526 a new automated single ring infiltrometer for Beerkan infiltration experiments.
527 *Geoderma* 262, 20–34. <http://dx.doi.org/10.1016/j.geoderma.2015.08.006>

528 Haverkamp, R., Ross, P.J., Smettem, K.R.J., Parlange, J.Y., 1994. 3-Dimensional analysis of
529 infiltration from the disc infiltrometer .2. Physically-based infiltration equation.
530 *Water Resources Research* 30, 2931–2935.

531 Klípa, V., Sněhota, M., Dohnal, M., 2015. New automatic minidisk infiltrometer: design and
532 testing. *Journal of Hydrology and Hydromechanics* 63.
533 <https://doi.org/10.1515/johh-2015-0023>

534 Lai, J., Ren, L., 2007. Assessing the Size Dependency of Measured Hydraulic Conductivity
535 Using Double-Ring Infiltrimeters and Numerical Simulation. *Soil Science Society of
536 America Journal* 71, 1667. <https://doi.org/10.2136/sssaj2006.0227>

537 Lassabatere, L., Angulo-Jaramillo, R., Soria Ugalde, J.M., Cuenca, R., Braud, I.,
538 Haverkamp, R., 2006. Beerkan estimation of soil transfer parameters through
539 infiltration experiments—BEST. *Soil Science Society of America Journal* 70, 521.
540 <https://doi.org/10.2136/sssaj2005.0026>

541 Lassabatere, L., Di Prima, S., Angulo-Jaramillo, R., Keesstra, S., Salesa, D., 2019a. Beerkan
542 multi-runs for characterizing water infiltration and spatial variability of soil hydraulic
543 properties across scales. *Hydrological Sciences Journal* 64, 165–178.
544 <https://doi.org/10.1080/02626667.2018.1560448>

545 Lassabatere, L., Di Prima, S., Bouarafa, S., Iovino, M., Bagarello, V., Angulo-Jaramillo, R.,
546 2019b. BEST-2K Method for Characterizing Dual-Permeability Unsaturated Soils
547 with Pondered and Tension Infiltrimeters. *Vadose Zone Journal* 18.
548 <https://doi.org/10.2136/vzj2018.06.0124>

549 Lozano-Baez, S.E., Cooper, M., Ferraz, S.F.B., Ribeiro Rodrigues, R., Pirastru, M., Di
550 Prima, S., 2018. Previous Land Use Affects the Recovery of Soil Hydraulic
551 Properties after Forest Restoration. *Water* 10. <https://doi.org/10.3390/w10040453>

552 Madsen, M.D., Chandler, D.G., 2007. Automation and Use of Mini Disk Infiltrometers. Soil
553 Science Society of America Journal 71, 1469.
554 <https://doi.org/10.2136/sssaj2007.0009N>

555 Milla, K., Kish, S., 2006. A low-cost microprocessor and infrared sensor system for
556 automating water infiltration measurements. Computers and Electronics in
557 Agriculture 53, 122–129. <https://doi.org/10.1016/j.compag.2006.05.001>

558 Moret, D., López, M.V., Arrúe, J.L., 2004. TDR application for automated water level
559 measurement from Mariotte reservoirs in tension disc infiltrometers. Journal of
560 Hydrology 297, 229–235. <https://doi.org/10.1016/j.jhydrol.2004.04.003>

561 Moret-Fernández, D., González, C., Lampurlanés, J., Vicente, J., 2012. An automated disc
562 infiltrometer for infiltration rate measurements using a microflowmeter.
563 Hydrological Processes 26, 240–245. <https://doi.org/10.1002/hyp.8184>

564 Nyman, P., Sheridan, G., Lane, P.N.J., 2010. Synergistic effects of water repellency and
565 macropore flow on the hydraulic conductivity of a burned forest soil, south-east
566 Australia. Hydrol. Process. 24, 2871–2887. <https://doi.org/10.1002/hyp.7701>

567 Prieksat, M.A., Ankeny, M.D., Kaspar, T.C., 1992. Design for an Automated,
568 Self-Regulating, Single-Ring Infiltrometer. Soil Science Society of America Journal
569 56, 1409. <https://doi.org/10.2136/sssaj1992.03615995005600050013x>

570 Reynolds, W., Elrick, D., 2002. 3.4.3.2.b Pressure infiltrometer. In Methods of Soil Analysis,
571 Part 4, Physical Methods, Dane JH, Topp GC (eds). SSSA Book Series, No. 5. Soil
572 Sci. Soc. Am.: Madison, Wisconsin, USA 4, 826–836.

573 Reynolds, W., Elrick, D., Youngs, E., 2002. 3.4.3.2 Ring or cylinder infiltrometers (vadose
574 zone). In Methods of Soil Analysis, Part 4, Physical Methods, Dane JH, Topp GC
575 (eds). SSSA Book Series, No. 5. Soil Sci. Soc. Am.: Madison, Wisconsin, USA 818–
576 820.

577 Reynolds, W.D., Elrick, D.E., 2002. 3.4.3.3 Constant Head Well Permeameter (Vadose
578 Zone), in: Methods of Soil Analysis: Part 4 Physical Methods, SSSA Book Series.
579 Soil Science Society of America, Madison, WI, pp. 844–858.
580 <https://doi.org/10.2136/sssabookser5.4.c33>

581 Reynolds, W.D., Elrick, D.E., 1990. Poned Infiltration From a Single Ring: I. Analysis of
582 Steady Flow. Soil Science Society of America Journal 54, 1233.
583 <https://doi.org/10.2136/sssaj1990.03615995005400050006x>

584 Selker, J.S., Suter, J.D., Cuenca, R.H., Flugstad, B.A., Kelly, S.F., 2009. Tension
585 infiltrometer enhancements with automated pneumatic control and more durable base
586 plate: ENHANCED TENSION INFILTRMETER. Water Resources Research 45,
587 n/a-n/a. <https://doi.org/10.1029/2008WR007075>

588 Stewart, R.D., Abou Najm, M.R., 2018. A Comprehensive Model for Single Ring Infiltration
589 II: Estimating Field-Saturated Hydraulic Conductivity. Soil Science Society of
590 America Journal 82, 558–567. <https://doi.org/10.2136/sssaj2017.09.0314>

591 Verbist, K., Torfs, S., Cornelis, W.M., Oyarzún, R., Soto, G., Gabriels, D., 2010.
592 Comparison of single- and double-ring infiltrometer methods on stony soils. Vadose
593 Zone Journal 9, 462–475. <https://doi.org/10.2136/vzj2009.0058>

594 Xu, X., Lewis, C., Liu, W., Albertson, J.D., Kiely, G., 2012. Analysis of single-ring
595 infiltrometer data for soil hydraulic properties estimation: Comparison of BEST and

596 Wu methods. *Agricultural Water Management* 107, 34–41.
597 <https://doi.org/10.1016/j.agwat.2012.01.004>

598 Yilmaz, D., Lassabatere, L., Angulo-Jaramillo, R., Deneele, D., Legret, M., 2010.
599 Hydrodynamic Characterization of Basic Oxygen Furnace Slag through an Adapted
600 BEST Method. *Vadose Zone Journal* 9, 107. <https://doi.org/10.2136/vzj2009.0039>

601 Zimmermann, B., Zehe, E., Hartmann, N.K., Elsenbeer, H., 2008. Analyzing spatial data: An
602 assessment of assumptions, new methods, and uncertainty using soil hydraulic data:
603 ANALYZING SPATIAL DATA. *Water Resources Research* 44, n/a-n/a.
604 <https://doi.org/10.1029/2007WR006604>

605 Zumr, D., Jeřábek, J., Klípa, V., Dohnal, M., Sněhota, M., 2019. Estimates of Tillage and
606 Rainfall Effects on Unsaturated Hydraulic Conductivity in a Small Central European
607 Agricultural Catchment. *Water* 11, 740. <https://doi.org/10.3390/w11040740>
608

609

610 **Table 1.** Coordinates, dry soil bulk density, ρ_b (g cm^{-3}), and initial volumetric soil water content,
611 θ_i ($\text{cm}^3 \text{cm}^{-3}$) for the three sampled soils in France (sample size for each soil, $N = 4$). Standard deviations
612 are indicated in parentheses.

Site	ENTPE-1	ENTPE-2	DOUA
Coordinates	45°46'42.46"N	45°46'42.40"N	45°47'5.67"N
	4°55'33.68"E	4°55'30.62"E	4°52'17.31"E
ρ_b (g cm^{-3})	1.276 (0.150)	1.280 (0.154)	1.166 (0.043)
θ_i ($\text{cm}^3 \text{cm}^{-3}$)	0.378 (0.048)	0.400 (0.057)	0.273 (0.045)

613

614 **Table 2.** Calibration parameters of the ten infiltrometers.

Infiltrometer	1	2	3	4	5	6	7	8	9	10
Slope (V/mm H₂O)	0.00433	0.00435	0.00436	0.00435	0.00436	0.00433	0.00432	0.00433	0.00436	0.00435
Intercept (V)	0.366	0.346	0.371	0.353	0.354	0.390	0.383	0.347	0.328	0.337
R²	1.0000	0.9999	0.9999	0.9999	0.9998	0.9999	0.9999	0.9998	0.9998	0.9999

615

616 **Table 3.** Minimum (Min), maximum (Max), mean, and coefficient of variation (CV) of the root mean squared
617 differences, *RMSD* (mm), relative error, *Er* (%), and relative error, $|Er(I_{tot})|$ (%), of the total cumulative flow,
618 I_{tot} (mm), for the three procedures to treat the transducer output. Sample size for each procedure, $N = 10$.

Error	Data treatment	Min	Max	mean	CV (%)
<i>RMSD</i>	Manual selection	0.41	3.06	1.60 A	48.3
	Automatic selection	0.46	2.66	1.52 A	50.9
	Moving median	0.81	2.73	1.71 A	41.2
<i>Er</i>	Manual selection	0.28	2.06	1.06 A	48.2
	Automatic selection	0.31	1.83	1.02 A	50.5
	Moving median	0.52	1.77	1.11 A	40.5
$ Er(I_{tot}) $	Manual selection	0.11	1.41	0.79 A	47.8
	Automatic selection	0.29	1.76	0.86 A	53.3
	Moving median	0.06	1.60	0.86 A	63.9

619 For a given variable, means followed by the same letter are not significantly different according to a paired,
620 two-tailed t-test ($P < 0.05$).

621

622
623
624
625
626
627

Table 4. Parameter values for the three data treatment approaches (i.e., manual selection, automatic selection and moving median). and the four methods to estimate hydrodynamic parameters (i.e., BEST-slope, BEST-intercept, BEST-steady and Approach 4). k_{tot} is the total number of measured data points, i_s is the steady infiltration rate (mm h⁻¹), S is the soil sorptivity (mm h^{-0.5}), K_s is the saturated soil hydraulic conductivity (mm h⁻¹), k_{step} is the number of datapoints used to fit the model, and Er is the fitting error (%). Descriptive statistics are reported in bold.

Site	Statistic	k_{tot}	i_s	BEST-slope				BEST-intercept				BEST-steady		Approach 4	
				S	K_s	k_{step}	Er	S	K_s	k_{step}	Er	S	K_s	K_s	
Manual selection															
ENTPE-1		71	1512.5									55.9	1290.4	354.8	
		93	969.2	96.7	303.8	45	1.9	94.2	368.2	31	2.5	92.8 [†]	357.0 [†]	227.3	
		159	74.6											17.5	
		79	179.5	45.3	33.3	79	0.8	44.7	49.6	43	1.3	43.3	46.4	42.1	
		75	339.9	41.2	219.3	14	4.3	41.0	220.8	13	4.6	41.0	220.3	79.7	
		N	5	5	3	3	3	3	3	3	3	3	4	4	5
		mean	95.4	615.1	61.1	185.5	46.0	2.3	60.0	212.9	29.0	2.8	58.2	478.5	144.3
	CV (%)	38.3	99.2	50.7	74.6	70.7	76.8	49.5	74.9	52.1	59.3	41.1	116.2	99.2	
ENTPE-2		97	232.8	48.4	32.6	97	1.2	47.4	57.0	68	1.6	45.8	53.2	54.6	
		157	419.1					53.0	153.5	31	5.5	54.7	163.3	98.3	
		232	136.5					33.9	35.0	119	4.7	34.3	35.7	32.0	
		249	316.8	52.1	84.3	108	2.2	51.9	128.2	58	4.6	48.8	113.3	74.3	
		155	166.4	40.2	28.1	155	0.8	39.1	42.1	85	1.4	38.3	40.5	39.0	
		N	5	5	3	3	3	3	5	5	5	5	5	5	
		mean	178.0	254.3	46.9	48.4	120.0	1.4	45.1	83.1	72.2	3.5	44.4	81.2	59.7
	CV (%)	35.0	45.3	13.0	64.6	25.7	52.1	18.4	65.0	45.3	54.2	18.3	68.3	45.3	
DOUA															
		47	2684.4									101.3	2326.8	629.7	
		50	3129.0									111.4	2697.0	734.0	
	N	2	2									2	2	2	
	mean	48.5	2906.7									106.3	2511.9	681.8	
	CV (%)	4.4	10.8									6.7	10.4	10.8	
Automatic selection															
ENTPE-1		77	1511.9									50.2	1332.8	354.6	
		104	965.7	97.6	287.7	54	1.6	95.2	355.1	36	2.3	93.6 [†]	343.0 [†]	226.5	
		153	74.2											17.4	
		77	179.6	45.4	32.7	77	0.9	44.8	49.3	43	1.2	43.3	46.1	42.1	
		74	339.2	45.9	189.2	18	1.8	44.7	217.3	15	2.3	43.4	205.0	79.6	
		N	5	5	3	3	3	3	3	3	3	3	4	4	5
		mean	97.0	614.1	63.0	169.9	49.7	1.4	61.6	207.2	31.3	1.9	57.6	481.7	144.1
	CV (%)	34.6	99.2	47.6	75.7	59.9	34.9	47.3	73.9	46.5	32.3	41.9	120.4	99.2	
ENTPE-2		95	229.7	48.6	27.8	95	1.3	47.6	53.0	75	1.5	45.9	49.4	53.9	
		163	418.8					53.1	151.8	32	5.2	54.8	161.8	98.2	
		223	135.8					34.2	34.1	121	4.7	34.4	34.5	31.8	
		233	315.0	51.5	88.2	91	1.8	50.9	122.7	58	3.1	48.7	112.2	73.9	
		154	166.2	40.2	27.9	154	0.8	39.1	41.9	85	1.4	38.4	40.3	39.0	
		N	5	5	3	3	3	3	5	5	5	5	5	5	
		mean	173.6	253.1	46.7	48.0	113.3	1.3	45.0	80.7	74.2	3.2	44.4	79.6	59.4
	CV (%)	32.4	45.5	12.5	72.6	31.1	37.9	17.9	65.8	44.4	56.2	18.3	69.7	45.5	
DOUA															
		65	2680.1									111.4	2247.9	628.7	
		38	3113.5									75.9	2912.8	730.3	
	N	2	2									2	2	2	
	mean	51.5	2896.8									93.6	2580.4	679.5	
	CV (%)	37.1	10.6									26.8	18.2	10.6	
Moving median															
ENTPE-1		61	1529.8									53.4	1327.3	358.8	
		82	975.3	98.44	285.99	36	1.4	95.3	363.8	20	1.8	93.7 [†]	351.3 [†]	228.8	
		177	75.5											17.7	
		96	178.1	46.08	27.06	96	1.3	45.4	44.7	67	1.7	43.8	41.6	41.8	
		73	339.1	44.94	195.42	15	3.7	44.2	205.5	13	4.0	43.8	202.4	79.5	
		N	5	5	3	3	3	3	3	3	3	3	4	4	5
		mean	97.8	619.6	63.2	169.5	49.0	2.2	61.6	204.6	33.3	2.5	58.7	480.7	145.3
	CV (%)	47.1	99.6	48.4	77.5	85.8	62.2	47.4	78.0	88.1	51.7	40.5	120.3	99.6	
ENTPE-2		106	237.8	48.64	35.27	106	1.3	47.8	61.4	67	1.6	46.0	56.9	55.8	
		161	426.3	40.59	285.22	6	9.1	52.3	180.8	22	5.9	53.0	185.8	100.0	
		239	136.7	25.94	79.08	13	5.3	34.2	34.8	118	4.2	34.4	35.2	32.1	
		238	316.8	51.89	86.34	89	1.7	51.3	127.9	42	3.5	48.6	114.7	74.3	
		166	167.3	40.43	27.32	166	0.5	39.5	42.1	91	0.8	38.5	40.2	39.2	
		N	5	5	5	5	5	5	5	5	5	5	5	5	
		mean	182.0	257.0	41.5	102.6	76.0	3.6	45.0	89.4	68.0	3.2	44.1	86.5	60.3
	CV (%)	31.2	45.7	24.2	102.6	88.4	100.6	17.5	70.4	56.1	62.8	17.1	73.8	45.7	
DOUA															
		16	5215.1									231.3	3351.3	1223.3	
		22	4221.7									131.9	3615.3	990.3	
		35	2707.8									112.2	2268.9	635.2	
		30	3159.3									105.1	2774.2	741.1	
		27	3496.3									71.3 ^{††}	3319.2 ^{††}	820.1	
	N	5	5									5	5	5	
	mean	26.0	3760.0									130.4	3065.8	882.0	
	CV (%)	28.1	26.2									46.4	17.6	26.2	

628
629
630
631

N = sample size, CV = coefficient of variation.

[†] Values reported in Figure 6b.

^{††} Values reported in Figure 6g.

632 **Table 5.** Results of the single- and double-ring infiltration experiments.

Method	Water depth (mm)	Steady infiltration rate (mm h ⁻¹)	<i>K_s</i> (mm h ⁻¹)
Single-ring	25	105.8	43.6
	50	80.5	30.6
	75	73.3	25.8
Double-ring	25	22.7	22.7
	50	22.5	22.5
	75	15.0	15.0

633

634 **Figure 1.** Main components of the automatic system. (a) Box with differential pressure sensor MPXV5010DP;
635 (b) data acquisition system with Arduino MEGA 2560 Rev3; (c) 3D printed top and bottom plugs realized by
636 Multi Jet Fusion (MJF) printing technology; (d) Infiltrometer; (e) detailed scheme of the infiltrometer; (f) laser
637 cutting project for the realization of the (g) tripod and (*) support tubes. The project files for the manufacture of
638 the plugs and the tripod can be downloaded from the website bestsoilhydro.net.

639 **Figure 2.** (a) Sketch of the testing procedure; (b) weight of the discharged water and transducer output at time
640 immediately preceding two consecutive bubbling events; (c) manual selection of data at the end of the constant
641 height stages in Mariotte bottle; and (d) comparison between recorded and measured cumulative flow data.
642 Note that the recorded data in subpanel d were firstly converted into water column heights using the calibration
643 function for Infiltrometer #3, and then used to estimate infiltration amounts.

644 **Figure 3.** Automated infiltration experiments of the (a) single- and (b) double-ring type carried out respectively
645 at the DOUA site and at the Anand Agricultural University.

646 **Figure 4.** Experimental calibration curve of the MPXV5010DP sensor mounted on Infiltrometer #3. The
647 calibration multiplier is 4.36×10^{-3} V/mm H₂O ($R^2 = 1.0$). (∞) Recorded transducer outputs. (\sphericalangle) Visual
648 readings of the heights of the water column inside the Mariotte bottle during the complete emptying of the
649 reservoir.

650 **Figure 5.** Comparison between the errors obtained from the three procedures used to treat the transducer output.

651 **Figure 6.** Examples of transducer output for (a) stair-like data and (f) a rapid infiltration process. Subpanels c-e
652 present close views of the transducer readings reported in the gray rectangle of subpanel a and subpanels h-j
653 show close views of the readings reported in the gray rectangle of subpanel f. Note that the manual and
654 automatic procedures could not be applied to treat the raw data in case of rapid infiltration process (h and i)
655 owing to an uninterrupted air bubbling that spoiled the transducer readings. (b and g) Determined cumulative
656 infiltration amounts. The BEST-slope deduced S and K_s values are also reported. Note that the Mariotte bottles
657 were filled with tap water and then activated through lifting the pistons, at which time data acquisition began.
658 Then, the infiltration experiments started when the plastic films were removed. This procedure facilitated
659 accurate data acquisition from the beginning of the run, with a constant transducer output during the first
660 seconds of the experiments (x).

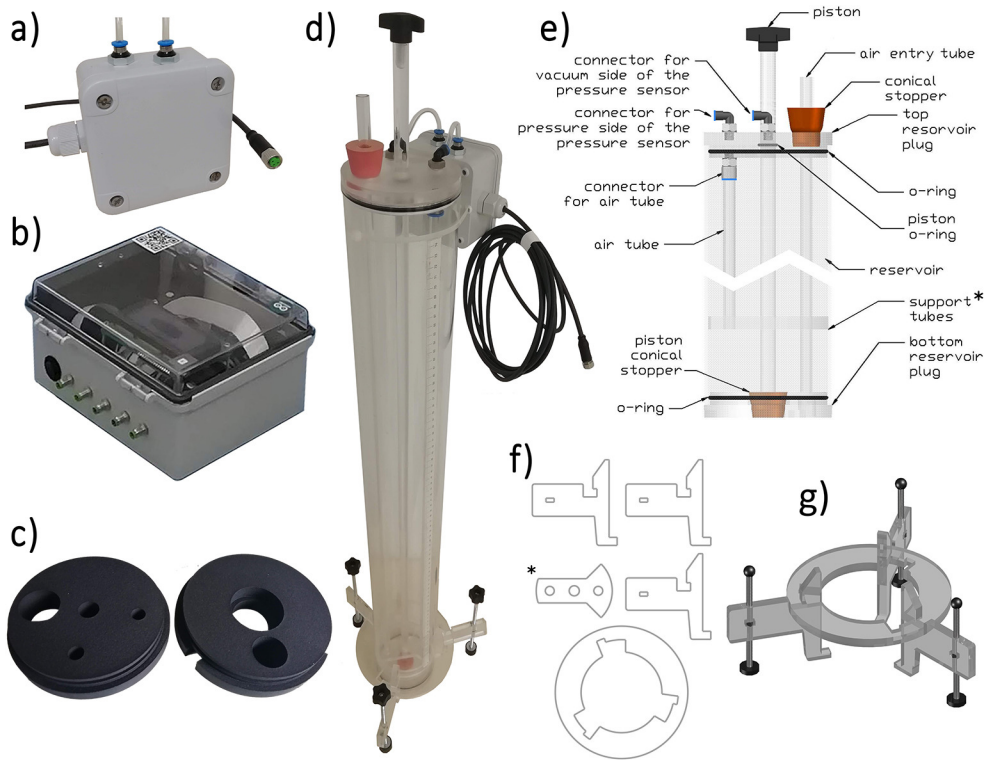
661 **Figure 7.** (a) Comparison between the success rates obtained for the three data treatments (i.e., manual
662 selection, MS, automatic selection AS, and moving median, MM), and the four methods for estimating the
663 hydrodynamic parameters (i.e., BEST-slope, BEST-intercept, BEST-steady and Approach 4). Box plots of the
664 (b) saturated soil hydraulic conductivity, K_s (mm h⁻¹), and (c) soil sorptivity, S (mm h^{-0.5}), pairs data for the
665 different scenarios. The sample size (N) for each box plot is also reported.

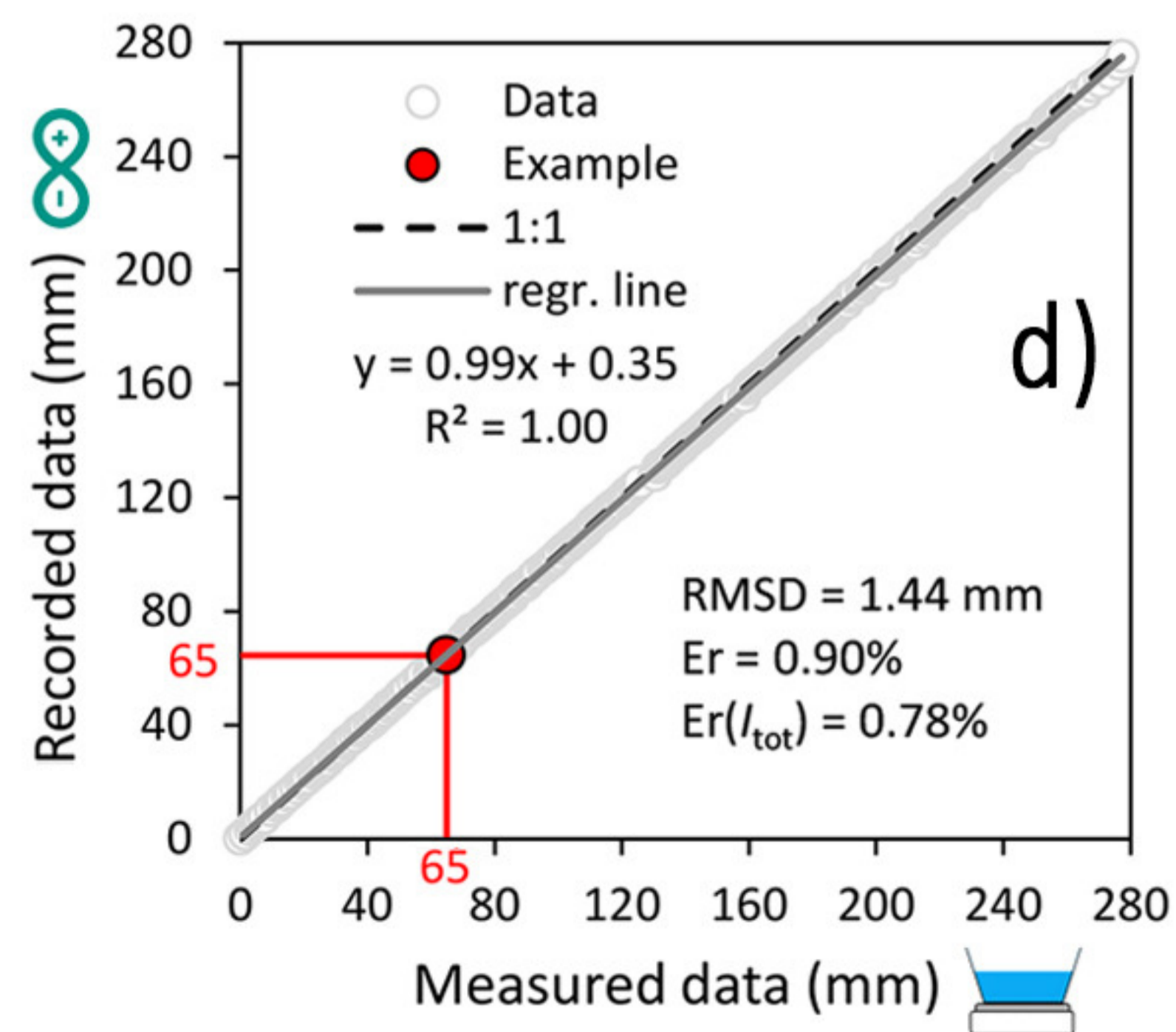
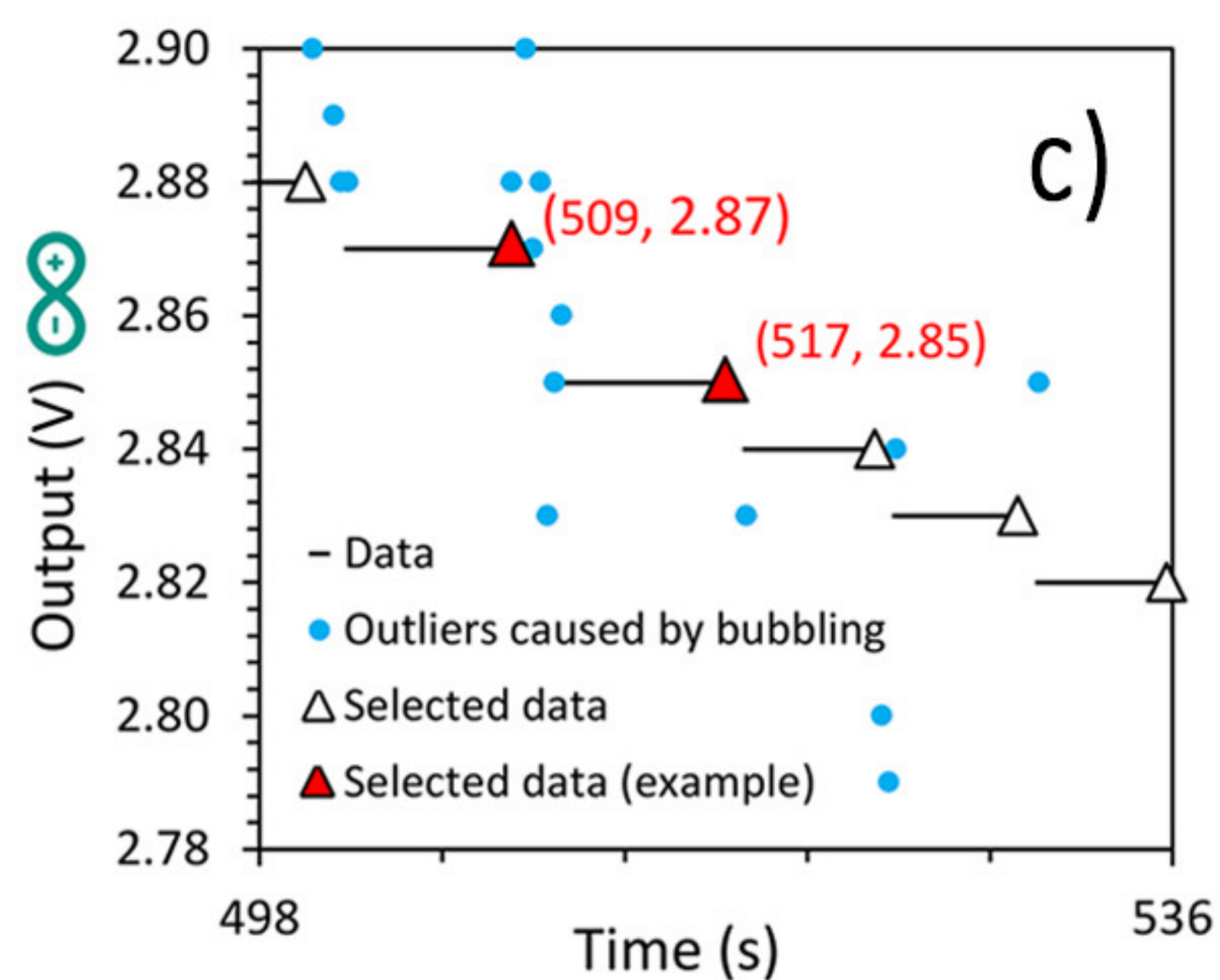
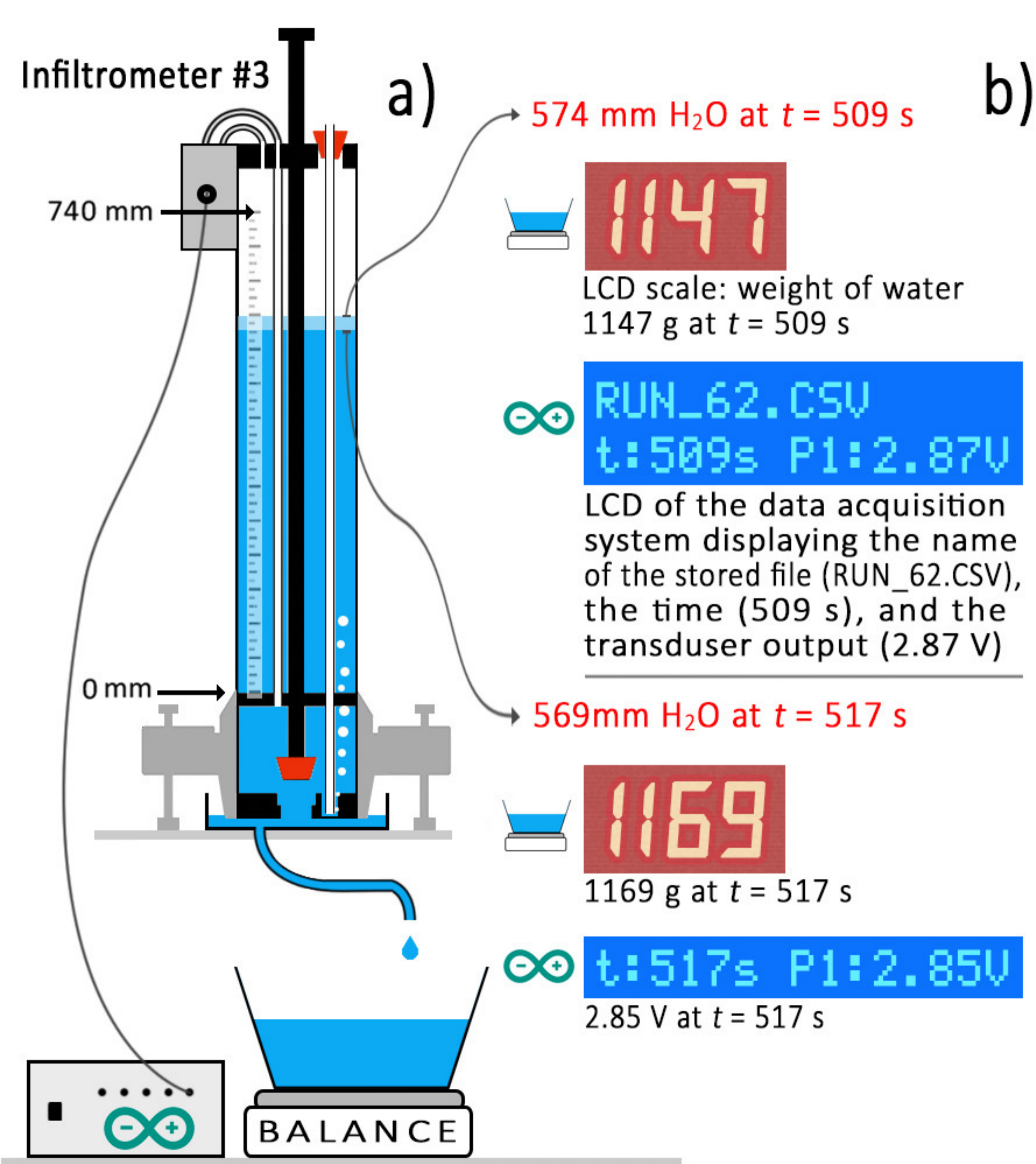
666 **Figure 8.** (a) Comparison between cumulative infiltration curves obtained from transducer output (open circles
667 \circ) and discretized data (solid circles \bullet). The solid line is the polynomial function used to model the discretized
668 data with the same increments as manually collected infiltration curves, i.e., 8.5 mm (“Beerkan-like data”). (b)
669 Infiltration rates of the discretized data. (c) Detailed view of the early-time infiltration stage. The dotted line is
670 the fitted cumulative infiltration model to the transient infiltration data. k_{step} is the number of datapoints used to
671 fit the model.

672 **Figure 9.** Comparison between cumulative infiltration curves collected with (a) the prototype proposed by Di
673 Prima (2015) on different soils analyzed during previous field campaigns (Di Prima, 2015; Di Prima et al.,
674 2017, 2016), versus (b) the curves collected with new infiltrometers at the ENTPE-1, ENTPE-2 and DOUA
675 sites. Subpanel c displays the interval plots with the mean values of the cumulative infiltration intervals, ΔI
676 (mm), and the 95% confidence interval bars. Individual standard deviations were used to calculate the intervals.

677 **Figure 10.** (a) Experimental setup consisting of ten infiltrometers working simultaneously and connected to
678 two data acquisition systems, and (b) measured cumulative infiltration curves.

679





a)



b)



